energies

MDPI

Article

Modeling and Analyzing the Effect of Frequency Variation on Weak Grid-Connected VSC System Stability in DC Voltage Control Timescale

Hui Yang * and Xiaoming Yuan

State Key Laboratory of Advanced Electromagnetic Engineering Technology, Huazhong University of Science and Technology, Wuhan 430074, China; yuanx@hust.edu.cn

* Correspondence: yanghui@hust.edu.cn; Tel.: +86-(0)27-8754-4359

Received: 16 September 2019; Accepted: 21 November 2019; Published: 22 November 2019

Abstract: The effect of frequency variation on system stability becomes crucial when a voltage source converter (VSC) is connected to a weak grid. However, previous studies lack enough mechanism cognitions of this effect, especially on the stability issues in DC voltage control (DVC) timescale (around 100 ms). Hence, this paper presented a thorough analysis of the effect mechanism of frequency variation on the weak grid-connected VSC system stability in a DVC timescale. Firstly, based on instantaneous power theory, a novel method in which the active/reactive powers are calculated with the time-varying frequency of voltage vectors was proposed. This method could intuitively reflect the effect of frequency variation on the active/reactive powers and could also help reduce the system order to a certain extent. Then, a small-signal model was established based on the motion equation concept, to depict the effect of frequency variation on the weak grid-connected VSC system dynamics. Furthermore, an analytical method was utilized to quantify the effect of frequency variation on the system's small-signal stability. The quantitative analysis considered the interactions between the DC voltage control, the terminal voltage control, phase-locked loop, and the power network. Finally, case studies were conducted, and simulation results supported the analytical analyses.

Keywords: frequency variation; weak grid; DC voltage control (DVC) timescale; motion equation; stability analysis; power calculation method; voltage source converter (VSC)

1. Introduction

In many parts of the world, including China, wind farms are often located far away from load centers [1]. Voltage source converters (VSCs) are widely used to connect wind power generation units to the grid in modern power systems. Integrating wind farms into the grid with long transmission lines will lead to VSCs connected to the weak grid, viz. short-circuit ratio (SCR < 3) [2]. VSC dynamics become more complicated when connected to the weak grid, which is often associated with stability issues [3] and considerable variation in converter-interface frequency [4,5]. In a report of general electric company [4], the frequency oscillation scenario was reported under weak-grid conditions. Additionally, it was concluded in reference [5] that the frequency variation can greatly affect the stability of distributed generation systems. Therefore, systematic analysis to reveal the effect mechanism of frequency variation on the weak grid-connected VSC system stability is urgently needed.

Many studies have been devoted to carrying out a thorough analysis of the effect mechanism of frequency variation on phase-locked loop (PLL)-synchronized VSC system stability. In references [6,7], a state-feedback PLL model is first proposed, and then the effect of frequency variation on system stability is described by a positive-feedback loop. It is concluded that the positive-feedback loop threatened the system's small-signal stability. In reference [8], it was found that the additional feedback

loop by frequency variation may have deteriorated the system's large-signal stability. In reference [9], an impedance-based VSC model was developed, and the effect of frequency variation on system stability was explored from the perspective of impedance interaction. It was concluded that the instability was a result of the negative incremental resistance behavior of the VSC's impedance. However, the above analyses mainly focused on the dynamics of the PLL, and the DC voltage control (DVC) dynamics were not included. Generally, the interactions between DVC, terminal voltage control and PLL—whose dynamics lie within the DVC timescale (around 100 ms)—become crucial under weak-grid conditions and could bring the corresponding stability problems [10]. Hence, a thorough analysis of the effect mechanism of frequency variation on the DVC timescale stability problems is also needed.

Some models that include DC voltage control dynamics could be utilized for dynamic analysis in DVC timescale. A state-space equation model is proposed in reference [11]. In reference [12], a grid-connected VSC system is modeled in the form of a closed-loop transfer function. However, those models may be lack of mechanism cognitions of the VSC's characteristics, e.g., the interactions of different control loops in VSC [13]. Then, a VSC model that contains the details of different control loops is established in [13] to reflect the VSC's characteristics. However, due to its complexity, this model is intractable to analyze the frequency dynamics and its effects on the stability in systems with multiple VSCs. To analyze the dynamics of power systems with large scale VSCs in DVC timescale, [14] proposes a small-signal model of VSC based on the motion equation concept. In this model, the self-characteristics of VSC are depicted by the relationship between the unbalanced active/reactive powers and the phase/amplitude dynamics of the VSC's internal voltage (viz. the output voltage of VSC). This modeling method has already been expanded for multi-VSC dynamic analysis in [15,16]. The form of this model resembles the rotor motion equation of the synchronous generator (SG) [17]. However, drawing lessons from conventional SG-dominated power systems, the reactance of the power network under the nominal frequency was utilized to calculate the active/reactive powers by references [14–16]. Owing to this nominal-frequency-based power calculation method, the existing motion-equation-concept models cannot depict the effect of frequency variation on the weak grid-connected VSC system dynamics.

The instantaneous power theory could be used to improve the nominal-frequency-based results, which has been effectively applied in the control algorithms of modern power electronic devices [18–21]. The existing calculation methods can be roughly divided into two categories. The first category calculates the active/reactive powers with the AC voltages/currents in $\alpha\beta$ coordinate [18,19], and the second category calculates the powers with the voltage/current in dq coordinate [20,21]. However, utilizing these methods to improve the nominal-frequency-based results will significantly increase the system order, especially for systems consisting of thousands of nodes [22]. Besides, due to the features of the chosen calculated variables, these methods are intractable to intuitively reflect the effect of frequency variation on the active/reactive powers, which may limit its flexibility when applied for further analysis of the effect of frequency variation on system stability.

In this vein, based on instantaneous power theory, this paper firstly proposes a novel method in which the active/reactive powers are calculated with the time-varying frequency of voltage vectors. The proposed power calculation method could intuitively reflect the effect of frequency variation on the active/reactive powers and can also help reduce the system order to a certain extent, which is applicable for further analysis of the effect of frequency variation on multi-VSC system stability in the DVC timescale. This is one main contribution of this paper. Then, a small-signal model is established based on the motion equation concept, to depict the effect of frequency variation on the weak grid-connected VSC system dynamics. Finally, an analytical method introduced in references [14,16] is utilized to quantify the effect of frequency variation on the system's small-signal stability. The quantitative analysis considers the interactions between the DVC, the terminal voltage control, PLL, and the power network. This is another main contribution of this paper.

The remaining parts of this paper are organized as follows. In Section 2, the studied grid-connected VSC system and the motion equation concept in DVC timescale are briefly introduced. Section 3 firstly

introduces the time-varying frequency of the VSC's internal voltage and then proposes a method to calculate the active/reactive powers with the time-varying frequency of voltage vectors. In Section 4, with the proposed power calculation method, a small-signal model is established based on the motion equation concept in order to depict the effect of frequency variation on the weak grid-connected VSC system dynamics. The effectiveness of the established model is verified through the simulation results and eigenvalue analysis. In Section 5, based on the established model, the quantitative analysis of the effect of frequency variation on the system's small-signal stability is conducted. Section 6 discusses the practicability of the proposed power calculation method in multi-VSC power systems, and Section 7 draws the conclusions.

2. Description of Grid-Connected VSC System and Motion Equation Concept in DVC Timescale

2.1. Description of Grid-Connected VSC System

Figure 1 depicts a simplified diagram of a grid-connected VSC utilizing a typical vector control scheme with terminal voltage vector oriented [21]. The output voltage of VSC (viz., the VSC's internal voltage) is produced from a DC voltage U_{dc} by pulse-width modulation (PWM) techniques. To eliminate current harmonics, the VSC is connected to the grid through a LC filter. And the grid is represented by an infinite voltage bus and a power transmission line.

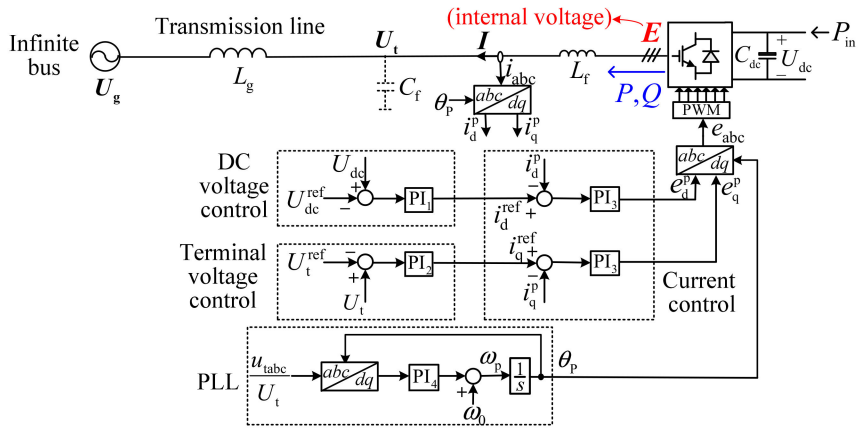

Figure 1. Typical diagram of a grid-connected voltage source converter (VSC) system. PI: Proportional-plus-integral; PWM: Pulse-width modulation.

The vector control scheme allows for decoupled control between active and reactive powers [21]. The active power control loop includes cascaded DVC and d-axis current (active power current component) control. DVC is aimed to balance the active power flowing through the DC capacitor and keep the DC voltage constant at the same time. The reactive power control includes terminal voltage control (TVC) and q-axis current (reactive power current component) control. TVC, as one scheme of the reactive power control, is adopted to maintain the terminal voltage within given values. Both active and reactive currents are controlled in a PLL-synchronized reference frame. PLL is used to capture the phase of terminal voltage as a synchronization signal employed by the transformations between *abc* and *dq* frames. A typical scheme of PLL is illustrated in Figure 1, and typical proportional-plus-integral (PI) regulators are applied in each VSC control loop.

2.2. Motion Equation Concept in DVC Timescale

2.2.1. Definition of DVC Timescale

For VSC control loops as introduced in Section 2.1, the response time constant of current control is often designed around 10ms (which is closely related to the switching frequency), and those of DVC, TVC, and PLL are selected to be about ten times larger [23]. Considering the designed response time

constant of different controllers, stability issues related to VSC can be classified into the DVC timescale stability problems [14–16,24] and the current control timescale stability problems [22,25]. For simplicity, the dynamics in these two timescales can be analyzed individually due to their relatively separated response times. Therefore, for stability analysis in the DVC timescale, AC currents can be considered to instantaneously track their reference values [14–16,24]. Besides, since the filter capacitor C_f mainly contributes to the high-frequency oscillations, which belong to the current control timescale [22,25], for stability analysis in the DVC timescale, the effect of the filter capacitor can be neglected [14–16,24].

2.2.2. Motion Equation Concept

The motion equation concept has already been used to describe the rotor dynamics of SGs in conventional SG-dominated power systems [17]. The basic rotor motion equation is shown in Figure 2a, where P_m and P_e are the mechanical and electromagnetic powers, ω_r and δ are the rotor speed and displacement of the rotor, ω_{SG} is the frequency of the SG's internal voltage, viz. back electromotive force (EMF). M_{SG} represents the rotor inertia, $K_{P\delta}$ represents the power network.

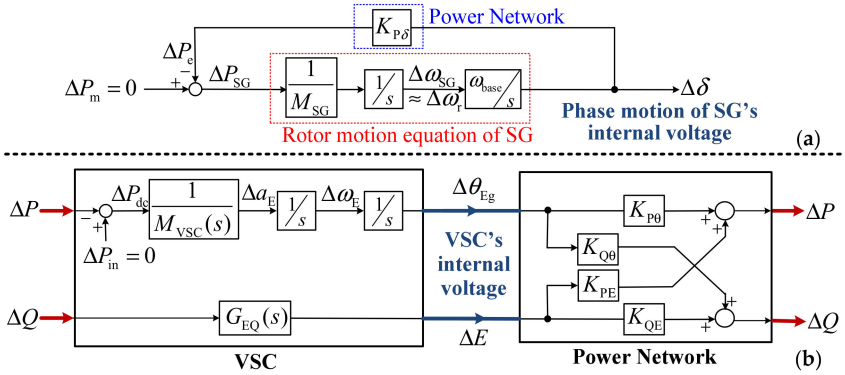

Figure 2. (**a**) Rotor motion equation of a synchronous generator (SG). (**b**) Previous proposed grid-connected VSC system model for stability analysis in DC voltage control (DVC) timescale based on the motion equation concept [14].

The motion equation concept can also be used to depict the characteristics of power electronics devices [14–16]. Previous proposed grid-connected VSC system model for stability analysis in DVC timescale based on the motion equation concept [14] is shown in Figure 2b. In this model, the internal voltage was chosen to describe the VSC's external characteristics. The inputs of the VSC model are the unbalanced active/reactive powers, and the phase/amplitude of the internal voltage are the outputs. The detailed modeling process is presented in Section 4.

A reasonable power calculation method is important to describe VSC's internal voltage dynamics in DVC timescale. In [14], the active/reactive powers are calculated with the network reactance under nominal frequency, which is also the modeling for power network. This nominal-frequency-based power network model is originated from conventional SG-dominated power systems. For SG's internal voltage, the nominal-frequency assumption is generally accepted due to the direct coupling between the rotor motion and back EMF, viz. $\Delta\omega_{SG} \approx \Delta\omega_r$ [17]. However, the dynamics of the VSC's internal voltage is greatly dependent on the fast controls. This difference may lead to the irrationality of the nominal-frequency assumption in VSC-dominated power systems, especially in a weak grid. In the next section, the time-varying frequency of VSC internal voltage will be introduced at first. Then, a novel power calculation method in which the effect of frequency variation is included will be proposed for improving the nominal-frequency-based results.

3. Proposed Power Calculation Method

In this section, we first introduced the time-varying frequency of the VSC's internal voltage. Then, a novel power calculation method in which the active/reactive powers are calculated with the

time-varying frequency of voltage vectors was proposed. The proposed power calculation method could conveniently improve the previous nominal-frequency-based results.

3.1. Time-Varying Frequency of VSC's Internal Voltage

The output voltage of the converter was defined as the VSC's internal voltage [14–16,25]. Its generation process was as follows. Firstly, based on a rotating reference frame employed by PLL, the control system generated d-axis component $e_{\mathrm{d}}^{\mathrm{p}}$ and q-axis component $e_{\mathrm{q}}^{\mathrm{p}}$, respectively. Then, according to $e_{\mathrm{d}}^{\mathrm{p}}$, $e_{\mathrm{q}}^{\mathrm{p}}$, and the synchronization signal θ_{p}, the modulation module synthesized the voltage vector $\boldsymbol{E}$. A vector diagram for VSC's internal voltage is shown in Figure 3.

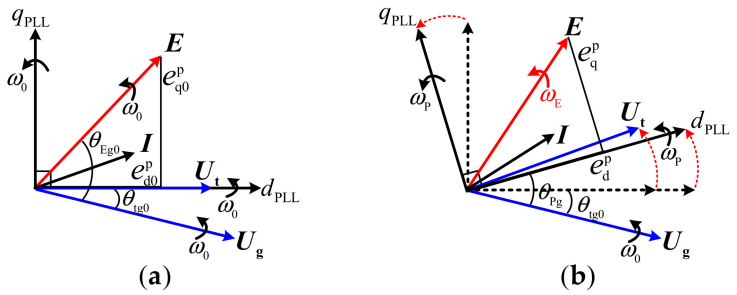

Figure 3. Vector diagram for the VSC's internal voltage. (**a**) At a steady state. (**b**) During the dynamic process. PLL: Phase-locked loop.

According to Figure 3, the amplitude and phase of VSC's internal voltage can be described as

$$E = \sqrt{e_{\mathrm{d}}^{\mathrm{p}2} + e_{\mathrm{q}}^{\mathrm{p}2}}, \tag{1}$$

$$\theta_{\mathrm{E}} = \arctan(e_{\mathrm{q}}^{\mathrm{p}}/e_{\mathrm{d}}^{\mathrm{p}}) + \theta_{\mathrm{P}}, \tag{2}$$

and the instantaneous frequency of the VSC's internal voltage is the differential of phase, which is:

$$\omega_{\mathrm{E}} = d\theta_{\mathrm{E}}/dt = d[\arctan(e_{\mathrm{q}}^{\mathrm{p}}/e_{\mathrm{d}}^{\mathrm{p}})]/dt + \omega_{\mathrm{P}}. \tag{3}$$

According to Figure 3a, at a steady state, the terminal voltage $\boldsymbol{U}_{\mathbf{t}}$ had the same phase with the d-axis of the PLL-synchronized reference frame. Assume that a disturbance occurs, making the terminal voltage vector lead the phase of steady-state situation, as shown in Figure 3b. Then, the PLL responded to capture the terminal voltage phase. Owing to the dynamics of PLL, the PLL frequency ω_{P} was not equal to the nominal frequency ω_0. Besides, the d-axis and q-axis internal voltage $e_{\mathrm{d}}^{\mathrm{p}}$, $e_{\mathrm{q}}^{\mathrm{p}}$ will be regulated by the DVC and TVC, respectively. According to Equation (3), the variation of ω_{P} and the regulation of $e_{\mathrm{d}}^{\mathrm{p}}$, $e_{\mathrm{q}}^{\mathrm{p}}$ all led to the frequency variation of VSC's internal voltage. Apart from the internal voltage, the frequency of terminal voltage vector also varied with time during dynamics. Thus, in the next section, a method in which the active/reactive powers were calculated with the time-varying frequency of voltage vectors is presented.

3.2. Power Calculation with the Time-Varying Frequency of Voltage Vectors

In order to calculate the active/reactive powers with the time-varying frequency of voltage vectors, several assumptions were made, which are listed as follows:

(1) The system is a symmetric 3-phase circuit;
(2) The power transmission line has lumped parameters, and the parameters are constant;
(3) The resistance and distributed capacitance in power transmission line are neglected.

The total instantaneous current flowing in the power transmission line was equal to the sum of instantaneous current produced by each voltage source separately, according to the superposition

theorem [26]. Thus, the instantaneous current produced by one voltage vector source $\boldsymbol{E_1}$ was calculated first, and the equivalent circuit is shown in Figure 4a. Note that voltage vector $\boldsymbol{E_1}$ here is a general expression of voltage vector, and it can represent both the VSC's internal voltage $\boldsymbol{E}$ and the terminal voltage $\boldsymbol{U_t}$.

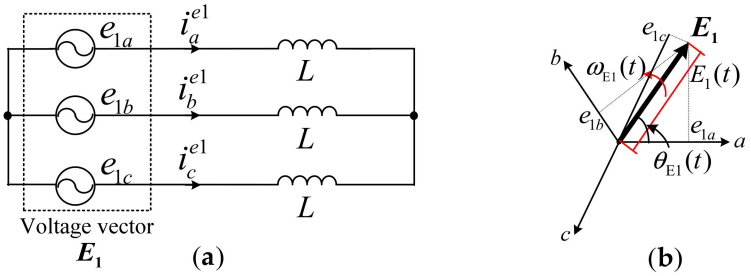

Figure 4. (**a**) Three-phase inductance circuit with voltage vector $\boldsymbol{E_1}$ as the source. (**b**) Spatial diagram of $\boldsymbol{E_1}$ and the instantaneous voltage in *abc* frame.

In Figure 4a, the instantaneous voltage of each phase in the *abc* frame was the projection of voltage vector $\boldsymbol{E_1}$, as shown in Figure 4b. Take phase *a* as an example, the instantaneous voltage e_{1a} is

$$e_{1a} = E_1(t)\cos(\int_{t_0}^{t}\omega_{E1}(t)dt + \theta_{E10}), \tag{4}$$

where θ_{E10} is the initial phase of voltage vector $\boldsymbol{E_1}$, which is constant. If the frequency of the voltage vector was regarded to be the nominal frequency ω_0, the instantaneous voltage in Equation (4) will become $e_{1a} = E_1(t)\cdot\cos(\omega_0 t + \theta_{E10})$.

The instantaneous voltage e_{1a} and instantaneous current i_a^{e1} satisfy the relationship as follows

$$i_a^{e1} - i_a^{e1}(t_0) = \frac{1}{L}\int_{t_0}^{t} e_{1a}dt = \frac{1}{L}\int_{t_0}^{t}[E_1(t)\cos(\int_{t_0}^{t}\omega_{E1}(t)dt + \theta_{E10})]dt, \tag{5}$$

where $i_a^{e1}(t_0)$ is the initial current. L is the total inductance of the circuit to be analyzed.

In order to obtain the analytical expression of the instantaneous current i_a^{e1} in Equation (5), the well-known integration by parts formulae in calculus are utilized. Then, i_a^{e1} can be described as follows:

$$i_a^{e1} - i_a^{e1}(t_0) = \frac{E_1(t)}{\omega_{E1}(t)L}\sin\theta_{E1}(t)\Big|_{t_0}^{t} - \frac{1}{L}\int_{t_0}^{t}\sin\theta_{E1}(t)d\frac{E_1(t)}{\omega_{E1}(t)}. \tag{6}$$

Continuing to apply the integration by parts to the second part on the right-hand side of Equation (7) gives

$$\int_{t_0}^{t}\sin\theta_{E1}(t)d\frac{E_1(t)}{\omega_{E1}(t)} = -\frac{1}{\omega_{E1}(t)}(\frac{E_1(t)}{\omega_{E1}(t)})'\cos\theta_{E1}(t)\Big|_{t_0}^{t} + \int_{t_0}^{t}\cos\theta_{E1}(t)d[\frac{1}{\omega_{E1}(t)}(\frac{E_1(t)}{\omega_{E1}(t)})'], \tag{7}$$

where the superscript ′ represents the differentiation of time for the function in brackets.

And so on, continuously applying the integration by parts to the calculated result. Neglecting the effect of the initial current $i_a^{e1}(t_0)$, current i_a^{e1} can be finally described with series including infinite elements, and it can be written as follows:

$$i_a^{e1} = I^1\sin\theta_{E1}(t) + [\sum_{k=1}^{\infty}(-1)^{k-1}I^{2k}]\cos\theta_{E1}(t) + [\sum_{k=1}^{\infty}(-1)^{k}I^{2k+1}]\sin\theta_{E1}(t), \tag{8}$$

where $I^1 = \frac{E_1(t)}{\omega_{E1}(t)L}, I^{k+1} = \frac{dI^k/dt}{\omega_{E1}(t)}k \in N_+$.

According to Equation (8), the original form of instantaneous current i_a^{e1} was extremely complex when described with the time-varying frequency of the voltage vector. Thus, appropriate simplification for the instantaneous current i_a^{e1} was needed. In Equation (8), the elements I^k, $k \geq 2$ were mainly determined by the differentiation of time for the voltage vector's amplitude/frequency and the total inductance L. The oscillation frequency was relatively low for the DVC timescale stability issues this paper was concerned with, thus the differentiation of time for the voltage vector's amplitude/frequency was small. Besides, in a weak grid, the power transmission line was long, thus the total inductance L was large. Thus, the elements I^k, $k \geq 2$ are quite small and can be neglected for stability analysis of the weak grid-connected VSC system in DVC timescale. Then, the instantaneous current i_a^{e1} can be described as follows:

$$i_a^{e1} = \frac{E_1(t)}{\omega_{\mathrm{E1}}(t)L} \sin \theta_{\mathrm{E1}}(t). \tag{9}$$

The form of Equation (9) is quite concise, and the effect of frequency variation can also be reflected since the time-varying frequency of the voltage vector $\omega_{\mathrm{E1}}(t)$ appears in Equation (9). If the frequency variation is neglected (adopted in reference [14]), the time-varying frequency $\omega_{\mathrm{E1}}(t)$ in Equation (9) needs to be replaced by ω_0. The reasonable simplification from Equation (8) to Equation (9) will also help simplify the stability analysis in an actual power system with multiple VSCs, which will be further discussed in Section 6. A two-node three-phase inductance circuit is chosen to calculate the active/reactive powers, as shown in Figure 5. The voltage vector $\boldsymbol{E_1}$ and $\boldsymbol{E_2}$ are the sources. Note that voltage vector $\boldsymbol{E_1}$, $\boldsymbol{E_2}$ here are general expressions of voltage vectors, and they can represent the VSC's internal voltage $\boldsymbol{E}$, the terminal voltage $\boldsymbol{U_t}$, or the infinite-bus voltage $\boldsymbol{U_g}$.

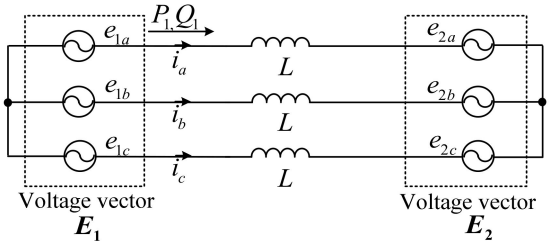

Figure 5. A two-node three-phase inductance circuit with voltage vectors $\boldsymbol{E_1}$ and $\boldsymbol{E_2}$ as the sources.

Substituting the amplitude/phase/frequency of $\boldsymbol{E_1}$ and $\boldsymbol{E_2}$ into Equation (9), respectively, the instantaneous current i_a can be described as follows:

$$i_a = \frac{E_1(t)}{\omega_{\mathrm{E1}}(t)L} \sin \theta_{\mathrm{E1}}(t) - \frac{E_2(t)}{\omega_{\mathrm{E2}}(t)L} \sin \theta_{\mathrm{E2}}(t). \tag{10}$$

Based on the instantaneous power theory [18], the 3-phase instantaneous active power P and reactive power Q can be calculated with the instantaneous voltage and instantaneous current in the *abc* frame. The calculation formulae are as follows:

$$P = u_a i_a + u_b i_b + u_c i_c, \tag{11}$$

$$Q = \frac{1}{\sqrt{3}}[(u_b - u_c)i_a + (u_c - u_a)i_b + (u_a - u_b)i_c], \tag{12}$$

where u_a, u_b, and u_c are the instantaneous voltage in each phase for a node. For node $\boldsymbol{E_1}$ in Figure 5, u_a, u_b, and u_c are equal to e_{1a}, e_{1b}, and e_{1c}, respectively. For node $\boldsymbol{E_2}$, u_a, u_b, and u_c are, respectively, equal to e_{2a}, e_{2b}, and e_{2c}. Since the 3-phase system is symmetric, the instantaneous current in the other 2 phases i_b and i_c can be obtained accordingly. Substituting the corresponding instantaneous voltage

and instantaneous current into Equations (11) and (12), the active/reactive power output of $\boldsymbol{E_1}$ can be obtained, respectively, which are denoted with P_1/Q_1:

$$P_1 = \frac{E_1(t)E_2(t)}{\omega_{E2}(t)L}\sin[\theta_{E1}(t) - \theta_{E2}(t)], \tag{13}$$

$$Q_1 = \frac{E_1^2(t)}{\omega_{E1}(t)L} - \frac{E_1(t)E_2(t)}{\omega_{E2}(t)L}\cos[\theta_{E1}(t) - \theta_{E2}(t)]. \tag{14}$$

Equations (13) and (14) are the calculated active/reactive powers with the proposed method in this paper. The calculated results are general expressions and can be applied to a 2-node 3-phase circuit for the calculation of active/reactive powers easily. For example, in the system in Figure 1, if $\boldsymbol{E_1}$ represents the VSC's internal voltage $\boldsymbol{E}$, $\boldsymbol{E_2}$ represents the terminal voltage $\boldsymbol{U_t}$, then L will be the filter inductance L_f. And if $\boldsymbol{E_1}$ represents the VSC's internal voltage $\boldsymbol{E}$, $\boldsymbol{E_2}$ represents the infinite-bus voltage $\boldsymbol{U_g}$, then L will be the total inductance $L_f + L_g$. The nominal-frequency-based results in reference [14] were equal to the results with the nominal frequency ω_0 replacing the time-varying frequency ω_{E1}(t), ω_{E2}(t) in Equations (13) and (14). Thus, the proposed power calculation method can further include the effect of frequency variation. Besides, Equations (13) and (14) describe the relationship between the active/reactive powers and the phase/amplitude of voltage vectors, which can be directly used for the power network modeling based on motion equation concept. Hence, in the next section, a small-signal model of the studied grid-connected VSC system will be established based on the motion equation concept, utilizing the proposed power calculation method.

4. System Modeling with the Proposed Power Calculation Method

In this section, a small-signal model of the studied grid-connected VSC system in Figure 1 was established based on the motion equation concept in order to depict the effect of frequency variation on the system dynamics. As introduced in Section 2.2.2, the VSC and the power network were modeled separately, with the internal voltage as the interface. For VSC modeling, firstly, a small-signal model was established to describe the VSC's internal voltage dynamics in DVC timescale, and then it was converted into a concise one based on the motion equation concept. For power network modeling, it can be derived easily with the proposed power calculation method. Finally, the effectiveness of the established model was verified through simulation results and eigenvalue analysis.

4.1. Small-Signal Modeling of VSC's Internal Voltage Dynamics in DVC Timescale

As introduced in Section 2.2.1, in the DVC timescale, the fast dynamics of current control loops were neglected for simplicity, which gives $i_d^{ref} \approx i_d^p$ and $i_q^{ref} \approx i_q^p$. Then, the relationship between control loops and the dynamics of internal voltage can be described as depicted in Figure 6.

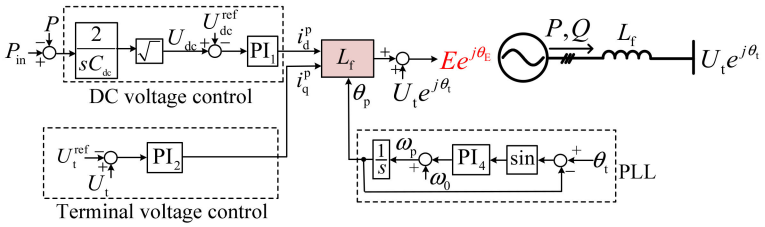

Figure 6. Relationship between control loops and the dynamics of internal voltage in the DVC timescale.

In the equivalent circuit of Figure 6, the active and reactive power outputs of VSC can be easily obtained with the proposed power calculation method. Substituting the corresponding amplitude/frequency/phase of the VSC's internal voltage $\boldsymbol{E}$ and the terminal voltage $\boldsymbol{U_t}$ into

Equations (13) and (14). And replacing L with the filter inductance L_f. Consequently, the active and reactive power outputs of the VSC are:

$$P = \frac{EU_t}{\omega_t L_f} \sin \theta_{Et}, \tag{15}$$

$$Q = \frac{E^2}{\omega_E L_f} - \frac{EU_t}{\omega_t L_f} \cos \theta_{Et}. \tag{16}$$

Then, the active and reactive current component i_p^E, i_q^E of the VSC's internal voltage can be calculated, respectively,

$$i_p^E = \frac{P}{E} = \frac{U_t}{\omega_t L_f} \sin \theta_{Et}, \tag{17}$$

$$i_q^E = \frac{Q}{E} = \frac{E}{\omega_E L_f} - \frac{U_t}{\omega_t L_f} \cos \theta_{Et}, \tag{18}$$

where the active current component i_p^E has the same phase as the VSC's internal voltage, and the reactive current component i_q^E leads or lags 90° with the internal voltage phase. According to the vector diagram in Figure 3, i_d^p and i_q^p can be described with i_p^E and i_q^E as follows:

$$i_d^p = i_p^E \cos(\theta_E - \theta_p) + i_q^E \sin(\theta_E - \theta_p), \tag{19}$$

$$i_q^p = i_p^E \sin(\theta_E - \theta_p) - i_q^E \cos(\theta_E - \theta_p). \tag{20}$$

Substituting Equations (17) and (18) into Equations (19) and (20), and then linearizing Equations (19) and (20), we get

$$\Delta i_d^p = -\frac{U_{t0}}{\omega_0 L_f} \Delta\theta_{tp} + \frac{E_0}{\omega_0 L_f} (\Delta\theta_{Eg} - \Delta\theta_{pg}), \tag{21}$$

$$\Delta i_q^p = \frac{\Delta U_t}{\omega_0 L_f} - \frac{\Delta E}{\omega_0 L_f} - \frac{U_{t0}}{{\omega_0}^2 L_f \omega_{base}} \Delta\omega_t + \frac{E_0}{{\omega_0}^2 L_f \omega_{base}} \Delta\omega_E. \tag{22}$$

Here, the initial power angle between the internal voltage and the terminal voltage $\delta_0 = \theta_{Eg0} - \theta_{tg0}$ is regarded to be small enough such that $\sin\delta_0 \approx 0$ and $\cos\delta_0 \approx 1$, which is also adopted in [14]. Additionally, $\Delta\omega_E = s\Delta\theta_{Eg}$, and $\Delta\omega_t = s\Delta\theta_{tg}$.

Equations related to DVC, TVC, and PLL are described in detail in [14]:

$$\Delta U_{dc} = \frac{1}{sC_{dc}U_{dc0}} (\Delta P_{in} - \Delta P), \tag{23}$$

$$\Delta i_d^p = (\Delta U_{dc} - \Delta U_{dc}^{ref})(k_{p1} + k_{i1}/s), \tag{24}$$

$$\Delta i_q^p = (\Delta U_t - \Delta U_t^{ref})(k_{p2} + k_{i2}/s), \tag{25}$$

$$\Delta\theta_{pg} = \Delta\theta_{tp}(k_{p4}/s + k_{i4}/s^2). \tag{26}$$

Based on Equations (21)–(26), the corresponding small-signal model to describe the dynamics of VSC's internal voltage can be described as shown in Figure 7. Therein, the black lines were consistent with the previous nominal-frequency-based model in reference [14], and the red lines were related to the effect of frequency variation.

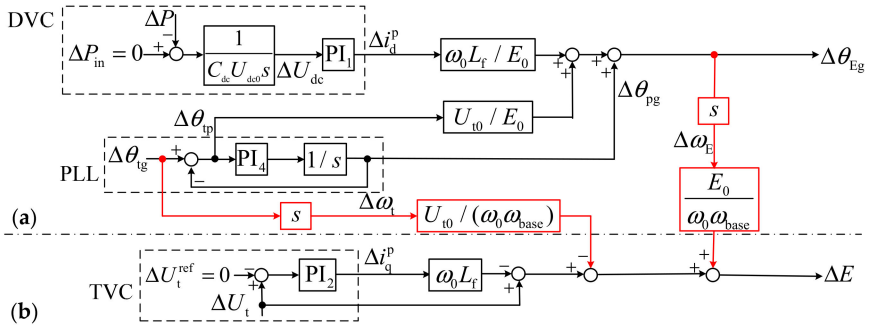

Figure 7. The small-signal model of VSC's internal voltage in DVC timescale. (**a**) Phase dynamics of VSC's internal voltage. (**b**) Amplitude dynamics of VSC's internal voltage.

4.2. Established VSC Model based on Motion Equation Concept

In Figure 7, the terminal voltage dynamics were determined not only by the VSC itself but also by all other devices in the grid, thus they cannot be used to describe VSC's self-characteristics. Hence, the terminal voltage dynamics should be replaced with VSC's own parameters. Through linearizing Equations (15) and (16), the terminal voltage phase and amplitude dynamics can be expressed as

$$\Delta\theta_{\mathrm{tg}} = \Delta\theta_{\mathrm{Eg}} - \frac{\omega_0 L_{\mathrm{f}}}{E_0 U_{\mathrm{t0}}}\Delta P, \tag{27}$$

$$\Delta U_{\mathrm{t}} = (\Delta E - \frac{E_0}{\omega_0\omega_{\mathrm{base}}}\Delta\omega_{\mathrm{E}} + \frac{U_{\mathrm{t0}}}{\omega_0\omega_{\mathrm{base}}}\Delta\omega_{\mathrm{t}}) + \frac{E_0 - U_{\mathrm{t0}}}{E_0}\Delta E - \frac{\omega_0 L_{\mathrm{f}}}{E_0}\Delta Q. \tag{28}$$

According to Equations (27) and (28), the block diagram of Figure 7 can be converted into the form depicted in Figure 8, where the variation of terminal voltage $U_{\mathrm{t}}e^{\mathrm{j}\theta\mathrm{t}}$ are equivalently replaced by the dynamics of powers P, Q, and internal voltage $Ee^{\mathrm{j}\theta\mathrm{E}}$, as indicated by the blue dotted lines. Then, the equivalent inertia $M_{\mathrm{VSC}}(s)$ for the phase motion of the VSC's internal voltage can be obtained, as shown in Figure 9a. In Figure 9a, the transfer function $G_{\mathrm{E}\omega}(s)$ describes the effect of frequency variation on the amplitude dynamics of VSC's internal voltage, which is not considered by [14]. The detailed expressions of $M_{\mathrm{VSC}}(s)$, $G_{\mathrm{EQ}}(s)$ and $G_{\mathrm{E}\omega}(s)$ are listed in Appendix A.

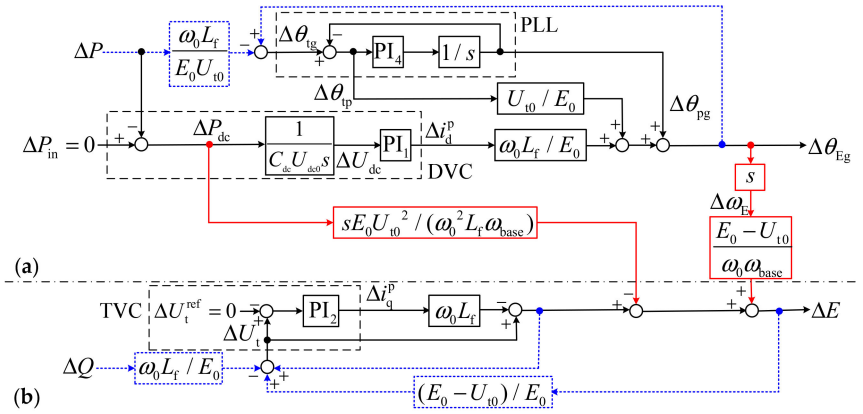

Figure 8. Replacing the variation of terminal voltage $U_{\mathrm{t}}e^{\mathrm{j}\theta\mathrm{t}}$ in Figure 7 with the dynamics of powers P, Q, and internal voltage $Ee^{\mathrm{j}\theta\mathrm{E}}$. (**a**) Phase dynamics of VSC's internal voltage. (**b**) Amplitude dynamics of VSC's internal voltage.

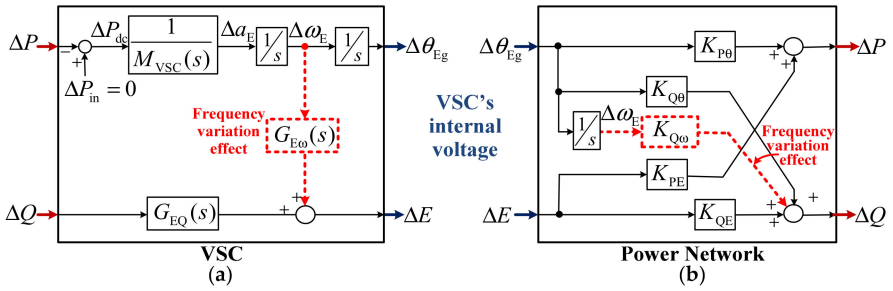

Figure 9. Established system model based on the motion equation concept. (**a**) VSC model. (**b**) Power network model.

4.3. Established Power Network Model

A small-signal power network model can be derived easily with the proposed power calculation method. Firstly, substituting the amplitude/phase/frequency of the internal voltage $\boldsymbol{E}$ and the infinite-bus voltage $\boldsymbol{U_g}$ into Equations (13) and (14), respectively, the active/reactive power output P/Q are

$$P = \frac{EU_g}{\omega_0 L}\sin\theta_{Eg}, \tag{29}$$

$$Q = \frac{E^2}{\omega_E L} - \frac{EU_g}{\omega_0 L}\cos\theta_{Eg}. \tag{30}$$

After linearizing Equations (29) and (30), the power network model is established, as depicted in Figure 9b,

$$\Delta P = \underbrace{\frac{U_g}{\omega_0 L}\sin\theta_{Eg0}}_{K_{PE}}\Delta E + \underbrace{\frac{E_0 U_g}{\omega_0 L}\cos\theta_{Eg0}}_{K_{P\theta}}\Delta\theta_{Eg} \tag{31}$$

$$\Delta Q = \underbrace{\frac{2E_0 - U_g\cos\theta_{Eg0}}{\omega_0 L}}_{K_{QE}}\Delta E + \underbrace{\frac{E_0 U_g\sin\theta_{Eg0}}{\omega_0 L}}_{K_{Q\theta}}\Delta\theta_{Eg} + \underbrace{\frac{-{E_0}^2}{\omega_0^2\omega_{base}L}}_{K_{Q\omega}}\Delta\omega_E \tag{32}$$

Combining the linear block diagram of the VSC and the power network, the small-signal model of the grid-connected VSC system in Figure 1 has been established, as depicted in Figure 9. Based on the established model, the effect of frequency variation on system dynamics in DVC timescale can be depicted. According to Figure 9, the frequency variation could affect the amplitude dynamics of the internal voltage through the control loops in VSC, which is described with $G_{E\omega}(s)$. The frequency variation could also affect the reactive power dynamics through the power network, which is described with $K_{Q\omega}$.

4.4. Verification of the Established Small-Signal Model

The effectiveness of the established model depicted in Figure 9 was verified by comparisons with the detailed model in MATLAB/SIMULINK and the previous nominal-frequency-based model. The parameters are listed in Appendix B. Assume that a small disturbance in the grid occurred at 2 s. Figure 10 shows the comparative responses of active/reactive power outputs P/Q between the established model, the previous model, and the detailed model. Here, P_{in} = 0.8 p.u. It was observed that responses of the established model were in good agreement with those of the detailed model, while the responses of the previous model deviated some from the detailed model. Figure 11a further compared the dominant eigenvalue locus of the established model and the previous model at varied grid strengths. It was observed that when L_g increases to 1 p.u., the dominant eigenvalue of the previous model enters the right-half plane, which means that the system was judged to be unstable.

However, the dominant eigenvalue of the established model in this paper was still in the left-half plane, which means that the system was judged to be stable. The established model became unstable after L_g increases to 1.01 p.u. Then, Figure 11b shows the simulation results of active power output P for the detailed model. According to Figure 11b, the actual stability of the system was the same as the conclusion judged via the established model in this paper but was different from that judged via the previous nominal-frequency-based model. Comparisons of simulation responses and eigenvalue analysis validated that the established model could hold the main behaviors of concern, even under weak grid conditions. The established model could depict the effect of frequency variation on the weak grid-connected VSC system dynamics in DVC timescale.

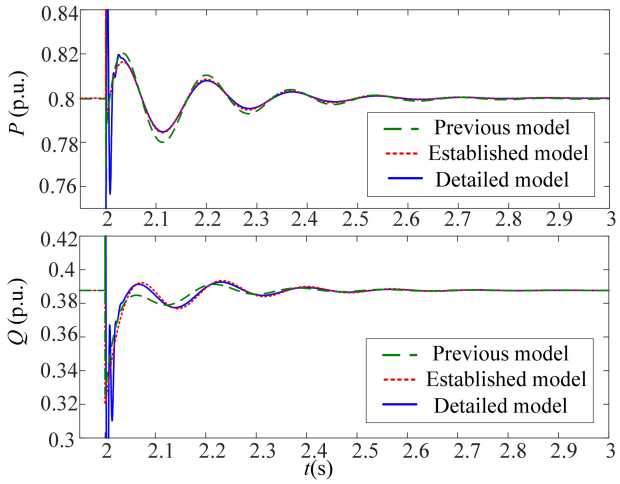

Figure 10. Comparisons of simulation responses between the established model, the previous nominal-frequency-based model, and the detailed model when the phase of $\boldsymbol{U_g}$ decreases 5° at 2s.

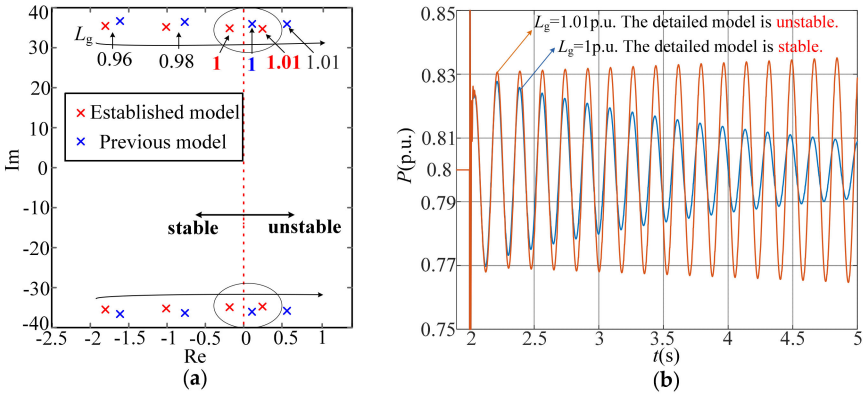

Figure 11. (**a**) Comparisons of dominant eigenvalue locus between the established model and the previous model at different grid strengths. (**b**) Responses of active power output P for the detailed model.

5. Effect Analysis of Frequency Variation on the System Stability in DVC Timescale

Based on the established model in Figure 9, this section presents a quantitative analysis of the effect of frequency variation on the system's small-signal stability. The quantitative analysis considered the interactions between the DVC, TVC, PLL, and the power network. Firstly, an analytical method introduced in references [14,16] was utilized to quantify the effect of frequency variation on the system's small-signal stability. Then, case studies were conducted under different controller parameters, and the effectiveness of the analytical analyses was verified through simulation results.

5.1. Stability Analysis of the Grid-Connected VSC System in Frequency Domain

The method introduced in references [14,16] can be used to analyze the small-signal stability of the system in Figure 9, by judging whether the system produces positive or negative damping at the oscillation frequency. According to Figure 9, the relationship between $\Delta\theta_{\mathrm{Eg}}$ and ΔE is

$$G_{\mathrm{E}\theta}(s) = \frac{K_{\mathrm{Q}\theta} G_{\mathrm{EQ}}(s)}{1 - K_{\mathrm{QE}} G_{\mathrm{EQ}}(s)}. \tag{33}$$

The relationships between $\Delta\omega_{\mathrm{E}}$ and ΔE include two kinds, one is related to the control loops in VSC, and another is related to the power network, which is denoted with $G_{\mathrm{E}\omega\text{-VSC}}(s)$ and $G_{\mathrm{E}\omega\text{-net}}(s)$:

$$G_{\mathrm{E}\omega-\mathrm{VSC}}(s) = \frac{G_{\mathrm{E}\omega}(s)}{1 - K_{\mathrm{QE}} G_{\mathrm{EQ}}(s)}, \tag{34}$$

$$G_{\mathrm{E}\omega-\mathrm{net}}(s) = \frac{K_{\mathrm{Q}\omega} G_{\mathrm{EQ}}(s)}{1 - K_{\mathrm{QE}} G_{\mathrm{EQ}}(s)}. \tag{35}$$

Based on Equations (33)–(35), the dynamics of amplitude can be equivalently converted into the VSC's phase motion, as shown in Figure 12.

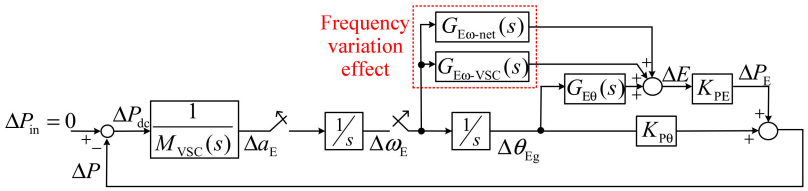

Figure 12. Converting the effect of amplitude dynamics into the VSC's phase motion (including the effect of frequency variation).

In Figure 12, the active power variation ΔP resulting from ΔE consisted of three branches, which affected the phase motion by the power network coupling. Two of these resulted from the frequency variation $\Delta\omega_{\mathrm{E}}$, and they represent the effect from the control loops in VSC and the effect from the power network, respectively, as indicated with the red dotted line. The remaining branch resulted from the phase variation $\Delta\theta_{\mathrm{Eg}}$. Through breaking the loop at the points in Figure 12, the frequency characteristics are calculated as:

$$\frac{\Delta a_{\mathrm{E}}}{\Delta\omega_{\mathrm{E}}} = -\frac{K_{\mathrm{PE}} G_{\mathrm{E}\theta}(s) + K_{\mathrm{P}\theta}}{s M_{\mathrm{VSC}}(s)} - \frac{K_{\mathrm{PE}}[G_{\mathrm{E}\omega-\mathrm{net}}(s) + G_{\mathrm{E}\omega-\mathrm{VSC}}(s)]}{M_{\mathrm{VSC}}(s)}, \tag{36}$$

where Δa_{E} is the dynamics of acceleration of the VSC's phase motion.

The stability of the system can be judged by Equation (36) with the following principle. If the real part of the transfer function $\Delta a_{\mathrm{E}}/\Delta\omega_{\mathrm{E}}(j\omega)$ in Equation (36) is negative, the system will produce positive damping, which means the system is stable; otherwise, the produced negative damping will lead to instability. This principle can be extended. The larger the real part of the transfer function $\Delta a_{\mathrm{E}}/\Delta\omega_{\mathrm{E}}(j\omega)$, the greater the negative damping produced by the system, the more unstable the system will be, and vice versa. According to the transfer function of Equation (36), the damping of the system can be divided into two parts. One part is the damping produced by the frequency variation itself, the other part is the damping produced by the phase variation (assume that the frequency is quasi-steady-state). It can be concluded that the controller parameters of TVC, DVC, PLL, the operating points, and the grid strengths all influence the characteristics of the term related to frequency variation's effect. The following case studies are given as examples to quantify the effect of frequency variation on the system's small-signal stability under different controller parameters.

5.2. Case Studies

5.2.1. Case Study 1: Effect of Frequency Variation under Different TVC Controller Parameters

Using the parameters listed in Appendix B, the frequency responses of $\mathrm{Re}[\Delta a_E/\Delta\omega_E(j\omega)]$ with different TVC controller parameters are illustrated, as shown in Figure 13. Note that the value of $\mathrm{Re}[\Delta a_E/\Delta\omega_E(j\omega)]$ is closely related to the oscillation frequency ω_d. Generally, a lower TVC bandwidth will result in a lower oscillation frequency of the analytical system, and the corresponding oscillation frequency in Figure 13 are ω_{d1} = 49.45 rad/s, ω_{d2} = 47.91 rad/s, and ω_{d3} = 46.15 rad/s. The solid lines consider the effect of frequency variation, while the dotted lines ignore it. The difference between the values of $\mathrm{Re}[\Delta a_E/\Delta\omega_E(j\omega_d)]$ resulting from considering and ignoring the frequency variation are $\Delta\mathrm{Re}(\omega_{d1})$ = 2.94, $\Delta\mathrm{Re}(\omega_{d2})$ = 7.75, $\Delta\mathrm{Re}(\omega_{d3})$ = 11.78, respectively. It is shown that the difference between them increased as the TVC bandwidth decreased. This means that a lower TVC bandwidth will result in a larger effect of frequency variation on the system stability. Furthermore, when the TVC controller parameter was set as (0.1, 6), $\mathrm{Re}[\Delta a_E/\Delta\omega_E(j\omega_{d3})] < 0$ when considering the effect of frequency variation. However, the conclusion under this set of parameters was the opposite when the effect of frequency variation was ignored, which indicates that the system was unstable.

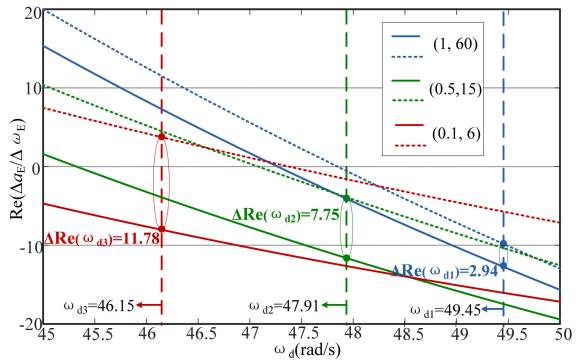

Figure 13. Impacts of different TVC controller parameters (k_{p2}, k_{i2}) on the frequency responses of the real part of the transfer function $\Delta a_E/\Delta\omega_E$. (The dotted lines are cases ignoring the effect of frequency variation, and the solid lines represent cases where it is considered. $\Delta\mathrm{Re}(\omega_d)$ is the difference between the values of $\mathrm{Re}[\Delta a_E/\Delta\omega_E(j\omega_d)]$ of them.).

Figure 14 shows the simulation responses of the VSC's internal voltage frequency ω_E for the detailed model. It was observed that a larger frequency variation of the VSC's internal voltage was associated with a lower TVC bandwidth. Besides, the system was stable when the TVC controller parameter was (0.1, 6), which was not consistent with the above analytical result when the effect of frequency variation was ignored. Therefore, the frequency variation had a great effect on the weak grid-connected VSC system's small-signal stability, especially with a lower TVC bandwidth.

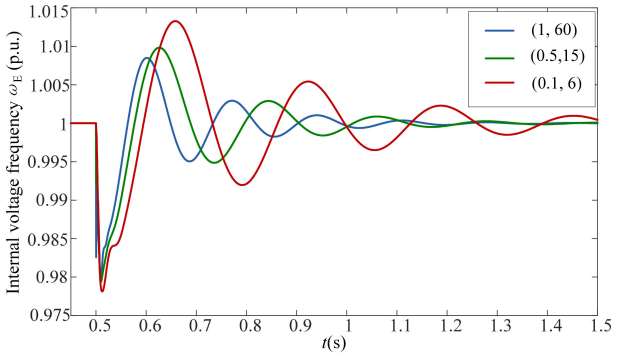

Figure 14. VSC internal voltage frequency dynamics with varied TVC controller parameters (k_{p2}, k_{i2}).

5.2.2. Case Study 2: Effect of Frequency Variation under Different PLL Controller Parameters

Using the parameters listed in Appendix B, the frequency responses of Re[$\Delta a_E/\Delta\omega_E(j\omega)$] with different PLL controller parameters are illustrated, as shown in Figure 15. The corresponding oscillation frequency in Figure 15 are ω_{d1} = 54.75 rad/s, ω_{d2} = 49.45 rad/s, and ω_{d3} = 45.87 rad/s. The solid lines consider the effect of frequency variation, while the dotted lines ignore it. The difference between the values of Re[$\Delta a_E/\Delta\omega_E(j\omega_d)$] resulting from considering and ignoring the frequency variation are ΔRe(ω_{d1}) = 3.83, ΔRe(ω_{d2}) = 2.73, ΔRe(ω_{d3}) = 1.98, respectively. It was shown that the difference between them became larger, with a higher PLL bandwidth when keeping the control loop's damping ratio constant. This means that a higher PLL bandwidth will result in a larger effect of frequency variation on the stability of a weak grid-connected VSC system. Figure 16 showed the simulation responses of VSC's internal voltage frequency ω_E for the detailed model. It was observed that a larger frequency variation of the VSC's internal voltage was associated with a higher PLL bandwidth. The simulation results supported the analytical results above.

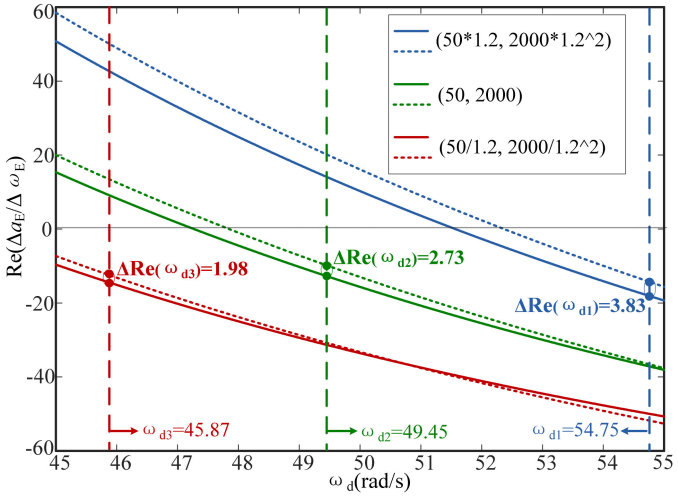

Figure 15. Impacts of different PLL controller parameters (k_{p4}, k_{i4}) on the frequency responses of the real part of the transfer function $\Delta a_E/\Delta\omega_E$. (The dotted lines are cases ignoring the effect of frequency variation, and the solid lines represent the cases where it is considered. ΔRe(ω_d) is the difference between the values of Re[$\Delta a_E/\Delta\omega_E(j\omega_d)$] of them.).

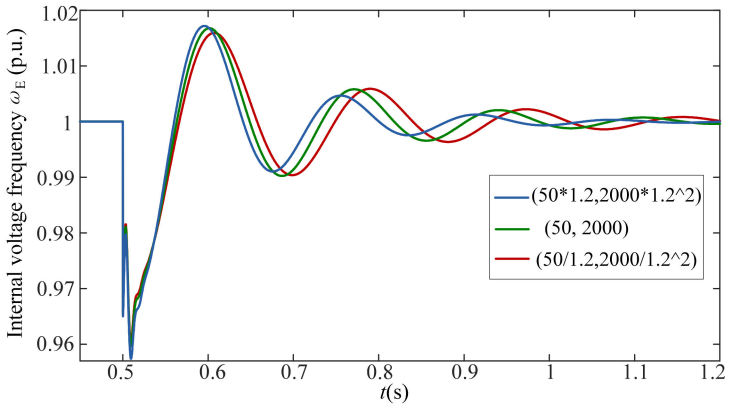

Figure 16. VSC internal voltage frequency dynamics with varied PLL controller parameters (k_{p4}, k_{i4}).

6. Discussion

In this section, the practicability of the proposed power calculation method in multi-VSC power systems is discussed. Take a power system consisting of n VSCs as an example. By collecting the information of the controller parameters and the operating points of each VSC, the small-signal model

of each VSC can be obtained, as shown in Figure 17. It is obvious that each VSC is interfaced with the grid through the amplitude/phase dynamics of the internal voltage. Through the superposition theorem, the active/reactive power outputs P_i/Q_i of each VSC can be calculated with the corresponding time-varying frequency of VSC's internal voltage replacing the nominal frequency, as described in Figure 17. The complete power network equations in the multi-VSC system can be described as a $n \times n$ matrix. Each element of the $n \times n$ matrix is a 2×2 matrix. Comparing with the previous nominal-frequency-based model in reference [14], the effect of frequency variation will increase the system order by about $2n$, including the n order brought by the power network matrix and the n order brought by the control loops in VSC $G_{E\omega i}(s)$.

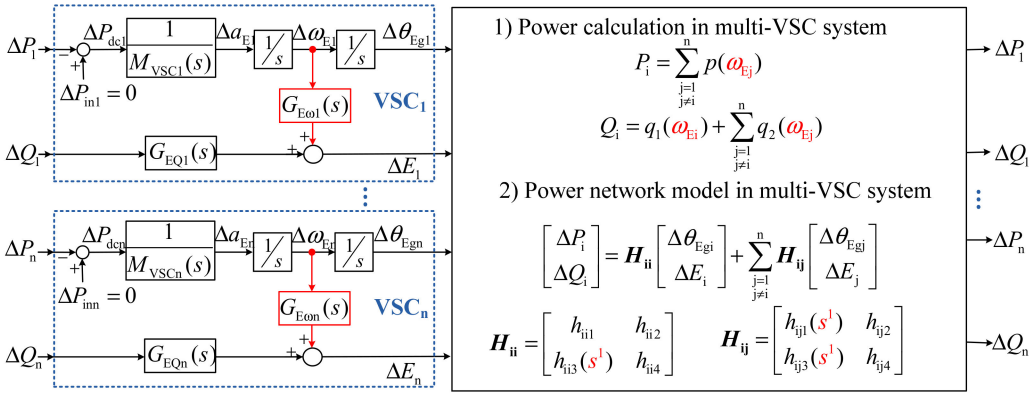

Figure 17. Schematic diagram of multi-VSC system modeling in DVC timescale with the proposed power calculation method.

Assume that the multi-VSC system consists of m inductors in the power network (including n filter inductors). For the existing instantaneous-power-theory-based method, the order of all inductors will be $2m - 2$, while it will be $2n$ for the proposed method in this paper, as stated above. Since the number of inductors is usually huge (viz. $m >> n$), the proposed method can help reduce the system order by about $2(m - n) - 2$. Thus, when the effect of frequency variation is regarded to be crucial for multi-VSC system stability analysis, the proposed method may be a better choice to improve the nominal-frequency-based results. Note that the proposed power calculation method just aims to analyze the stability problems in the DVC timescale. For the stability problems in the current control timescale, the simplification may be irrational since the elements I^k, $k \geq 2$ may be comparable with the element I^1. It is a follow-up goal to further verify the established model through the experimental results. Besides, the power calculation scenarios are relatively simple since the capacitances and resistances are neglected. A more general situation for power calculation is currently under study and will be published in the near future.

7. Conclusions

This paper presented a thorough analysis of the effect mechanism of frequency variation on the weak grid-connected VSC system stability in the DVC timescale. To achieve this goal, firstly, a novel method in which the active/reactive powers are calculated with the time-varying frequency of voltage vectors was proposed. The calculated results could intuitively reflect the effect of frequency variation on the active/reactive powers and could also help reduce the system order to a certain extent. Thus, the proposed method was applicable for further analysis of the effect of frequency variation on multi-VSC system stability. This was one main contribution of this paper. Secondly, a small-signal model was established based on the motion equation concept, to depict the effect of frequency variation on the weak grid-connected VSC system dynamics in the DVC timescale. It was found that the frequency variation affected the amplitude dynamics of the VSC's internal voltage through the interactions between the control loops in VSC, and also affected the reactive power dynamics through

the interactions with the power network. Comparisons of simulation responses and eigenvalue analysis validated that the established model could hold the main behaviors of concern, even under weak grid conditions. Then, an analytical method was utilized to quantify the effect of frequency variation on the system's small-signal stability. This quantitative analysis considered the interactions between the DVC, the TVC, PLL, and the power network. This was another main contribution of this paper. Case studies were conducted under different controller parameters, and simulation results supported the analytical analyses. The follow-up goals are to further verify the established model through the experimental results and to expand the proposed power calculation method for a more general situation.

Author Contributions: H.Y. and X.Y., proposed the main idea of the paper. H.Y. also implemented the mathematical derivations and simulation analyses. The paper is written by H.Y. and is revised by X.Y.

Funding: This research was funded by the National Natural Science Foundation of China (NSFC)- State Grid Corporation of China jointly under grant (U1766202). And this research was also funded by the National Key Research and Development Program of China (Grant number 2017YFB0902000).

Acknowledgments: The authors would like to thank Qi Hu from the National Key Laboratory of Science and Technology on Vessel Integrated Power System, Navy University of Engineering, for his help on the paper.

Conflicts of Interest: The authors declare no conflict of interest.

Nomenclature

P_{in}	Active power input of VSC
P, Q	Active and reactive power output of VSC
E, U_t, U_g	VSC's internal voltage, terminal voltage and infinite-bus voltage vectors
E, θ_E, ω_E	VSC's internal voltage amplitude, phase, and frequency
U_t, θ_t, ω_t	Terminal voltage amplitude, phase, and frequency
U_g, θ_g	Infinite-bus voltage amplitude and phase
I	Current vector
ω_p, θ_p	PLL frequency and output angle
$e_d{}^p$, $e_q{}^p$	Direct-axis and quadrature-axis current control output in PLL-synchronized reference frame
$i_d{}^p$, $i_q{}^p$	Direct-axis and quadrature-axis current components in PLL-synchronized reference frame
U_{dc}	DC voltage
L_f	VSC filter inductance
L_g	Transmission line inductance
$PI_j = k_{pj}+k_{ij}/s$	Transfer function of a generic PI controller (j = 1, 2, … ,4)
θ_{xy}	Difference of phase θ_x and phase θ_y
Superscript:	
ref	Reference value
Subscripts:	
abc	Components in *abc* frame
0	Initial values in steady-state condition

Appendix A. The Expressions of $M_{VSC}(s)$, $G_{EQ}(s)$ and $G_{E\omega}(s)$

$$M_{VSC}(s) = \frac{(E_0 - U_{t0})/(\omega_0 L_f)}{\frac{s^2}{E_0} + (\frac{k_{p1}}{C_{dc}U_{dc0}} + \frac{k_{p4}}{U_{t0}})s + \frac{(k_{i1}k_{p4}+k_{p1}k_{i4})s^{-1}}{C_{dc}U_{dc0}} + \frac{k_{i1}k_{i4}s^{-2}}{C_{dc}U_{dc0}} + \frac{k_{i1}+k_{p1}k_{p4}}{C_{dc}U_{dc0}} + \frac{k_{i4}}{U_{t0}}} \tag{A1}$$

$$G_{EQ}(s) = \frac{(\omega_0 L_f k_{p2} - 1)s + \omega_0 L_f k_{i2}}{[(2E_0 - U_{t0})k_{p2} - (2E_0 - U_{t0})/(\omega_0 L_f)]s + (2E_0 - U_{t0})k_{i2}} \tag{A2}$$

$$G_{E\omega}(s) = \frac{E_0(E_0 - U_{t0})(k_{p2}s + k_{i2}) - M_{VSC}(s)s^2[(\omega_0 L_f k_{p2} - 1)s + \omega_0 L_f k_{i2}]}{[(2E_0 - U_{t0})\omega_0\omega_{base}k_{p2} - (E_0 - U_{t0})\omega_{base}/L_f]s + (2E_0 - U_{t0})\omega_0\omega_{base}k_{i2}} \tag{A3}$$

Appendix B. 2-MW Grid-Connected VSC System Parameters

S_{base}= 2 MW	U_{base} = 690 V(phase to phase RMS value)	
$\omega_{base} = 2\pi f_{base}$	f_{base} = 50 Hz	U_{dcbase} = 1200 V
U_{dc}^{*} = 1 p.u.	C_{dc} = 0.1 F	U_{t}^{*} = 1 p.u.
U_g = 1 p.u.	L_f= 0.1 p.u.	L_g= 0.85 p.u.
Controller parameter values (p.u.)		
DC voltage control	k_{p1} = 3.5	k_{i1} = 140
Terminal voltage control	k_{p2} = 1	k_{i2} = 60
Current control	k_{p3} = 1.2	k_{i3} = 300
PLL control	k_{p4} = 50	k_{i4} = 2000

References

1. Piwko, R.; Miller, N.; Sanchez-Gasca, J.; Yuan, X.; Dai, R.; Lyons, J. Integrating large wind farms into weak power grids with long transmission lines. In Proceedings of the IEEE PES Transmission and Distribution Conference and Exposition, Asia and Pacific, Dalian, China, 18 August 2005; pp. 1–7.
2. Committee, D. *IEEE Guide for Planning DC Links Terminating at AC Locations Having Low Short-Circuit Capacities*; IEEE: New York, NY, USA, 1997; pp. 1–214.
3. Diedrichs, V.; Beekmann, A.; Busker, K.; Nikolai, S.; Adloff, S. Control of wind power plants utilizing voltage source converter in high impedance grids. In Proceedings of the IEEE PES General Meeting, San Diego, CA, USA, 22–26 July 2012; pp. 1–9.
4. Ye, Z.; Walling, R.; Garces, L.; Zhou, R.; Li, L.; Wang, T. *Study and Development of Anti-Islanding Control for Grid-connected Inverters*; National Renewable Energy Laboratory: Golden, CO, USA, 2004; pp. 1–82.
5. Wang, X.; Freitas, W. Impact of positive-feedback anti-islanding methods on small-signal stability of inverter-based distributed generation. *IEEE Trans. Energy Convers.* **2008**, *23*, 923–931. [CrossRef]
6. Dong, D.; Li, J.; Boroyevich, D.; Mattavelli, P.; Cvetkovic, I.; Xue, Y. Frequency behavior and its stability of grid-interface converter in distributed generation systems. In Proceedings of the Applied Power Electronics Conference & Exposition, Orlando, FL, USA, 5–9 February 2012; pp. 1887–1893.
7. Dong, D.; Wen, B.; Mattavelli, P.; Boroyevich, D.; Xue, Y. Grid-synchronization modeling and its stability analysis for multi-paralleled three-phase inverter systems. In Proceedings of the Applied Power Electronics Conference & Exposition, Long Beach, CA, USA, 17–21 March 2013; pp. 439–446.
8. Hu, Q.; Fu, L.; Ma, F.; Ji, F. Large signal synchronizing instability of PLL-based VSC connected to weak AC grid. *IEEE Trans. Power Syst.* **2019**, *34*, 3220–3229. [CrossRef]
9. Wen, B.; Dong, D.; Boroyevich, D.; Mattavelli, P.; Burgos, R.; Shen, Z. Impedance-based analysis of grid-synchronization stability for three-phase paralleled converters. In Proceedings of the Applied Power Electronics Conference & Exposition, Fort Worth, TX, USA, 16–20 March 2014; pp. 1233–1239.
10. Huang, Y.; Yuan, X.; Hu, J.; Zhou, P. Modeling of VSC connected to weak grid for stability analysis of DC-link voltage control. *IEEE J. Emerg. Sel. Top. Power Electron.* **2015**, *3*, 1193–1204. [CrossRef]
11. Kalcon, G.O.; Adam, G.P. Small-signal stability analysis of multi-terminal VSC-based DC transmission systems. *IEEE Trans. Power Syst.* **2012**, *27*, 1818–1830. [CrossRef]
12. Stamatiou, G.; Bongiorno, M. Stability analysis of two-terminal VSC-HVDC systems using the net-damping criterion. *IEEE Trans. Power Del.* **2016**, *31*, 1748–1756. [CrossRef]
13. Hu, J.; Huang, Y.; Wang, D.; Yuan, H.; Yuan, X. Modeling of grid-connected DFIG-based wind turbines for DC-link voltage stability analysis. *IEEE Trans. Sustain. Energy.* **2015**, *6*, 1325–1336. [CrossRef]
14. Yuan, H.; Yuan, X.; Hu, J. Modeling of grid-connected VSCs for power system small-signal stability analysis in DC-link voltage control timescale. *IEEE Trans. Power Syst.* **2017**, *32*, 3981–3991. [CrossRef]
15. Hu, J.; Yuan, H.; Yuan, X. Modeling of DFIG-based WTs for small-signal stability analysis in DVC timescale in power electronized power system. *IEEE Trans. Energy Convers.* **2017**, *32*, 1151–1165. [CrossRef]
16. Zheng, W.; Hu, J.; Yuan, X. Modeling of VSCs considering input and output active power dynamics for multi-terminal HVDC interaction analysis in DC voltage control timescale. *IEEE Trans. Energy Convers.* to be published. [CrossRef]
17. Kundur, P. *Power System Stability and Control*; McGraw-Hill: New York, NY, USA, 1994.

18. Akagi, H.; Kanazawa, Y.; Nabae, A. Instantaneous reactive power compensators comprising switching devices without energy storage components. *IEEE Trans. Ind. Appl.* **1984**, *IA-20*, 625–630. [CrossRef]
19. Akagi, H.; Nabae, A. The p-q theory in three-phase systems under non-sinusoidal conditions. *Eur. Trans. Elec. Power.* **1993**, *3*, 27–31. [CrossRef]
20. Ferrero, A.; Superti-Furga, G. A new approach to the definition of power components in three-phase systems under nonsinusoidal conditions. *IEEE Trans. Instrum. Meas.* **1991**, *40*, 568–577. [CrossRef]
21. Chinchilla, S.; Arnaltes, S.; Burgos, J.C. Control of permanent-magnet generators applied to variable-speed wind-energy systems connected to the grid. *IEEE Trans. Energy Convers.* **2006**, *21*, 130–135. [CrossRef]
22. Li, S.; Yan, Y.; Yuan, X. SISO equivalent of MIMO VSC-dominated power systems for voltage amplitude and phase dynamic analyses in current control timescale. *IEEE Trans. Energy Convers.*. to be published. [CrossRef]
23. Harnefors, L.; Bongiorno, M.; Lundberg, S. Input-admittance calculation and shaping for controlled voltage-source converters. *IEEE Trans. Ind. Electron.* **2007**, *54*, 3323–3334. [CrossRef]
24. Huang, Y.; Zhai, X.; Hu, J.; Liu, D.; Lin, C. Modeling and stability analysis of VSC internal voltage in DC-Link voltage control time scale. *IEEE J. Emerg. Sel. Top. Power Electron.* **2018**, *6*, 16–28. [CrossRef]
25. Yan, Y.; Yuan, X.; Hu, J. Stationary-frame modeling of VSC based on current-balancing driven internal voltage motion for current control timescale dynamic analysis. *Energies* **2018**, *11*, 438.
26. Robbins, A.H.; Miller, W.C. *Circuit Analysis: Theory and Practice*, 5th ed.; Cengage Learning: Boston, MA, USA, 2013.